APSB
Acta Pharmaceutica Sinica B

2020
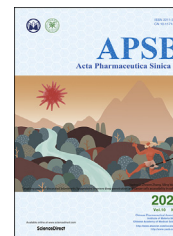
ORIGINAL ARTICLE

Targeting peptide-decorated biomimetic lipoproteins improve deep penetration and cancer cells accessibility in solid tumor

Tao Tan[a,†], Yuqi Wang[a,†], Jing Wang[b], Zhiwan Wang[b], Hong Wang[b], Haiqiang Cao[b], Jie Li[b], Yaping Li[b,c,*], Zhiwen Zhang[b,c,*], Siling Wang[a,*]

[a]School of Pharmacy, Shenyang Pharmaceutical University, Shenyang 110016, China
[b]State Key Laboratory of Drug Research & Center of Pharmaceutics, Shanghai Institute of Materia Medica, Chinese Academy of Sciences, Shanghai 201203, China
[c]Yantai Key Laboratory of Nanomedicine & Advanced Preparations, Yantai Institute of Materia Medica, Yantai 264000, China

Abstract The limited penetration of nanoparticles and their poor accessibility to cancer cell fractions in tumor remain essential challenges for effective anticancer therapy. Herein, we designed a targeting peptide-decorated biomimetic lipoprotein (termed as BL-RD) to enable their deep penetration and efficient accessibility to cancer cell fractions in a tumor, thereby improving the combinational chemo-photodynamic therapy of triple negative breast cancer. BL-RD was composed of phospholipids, apolipoprotein A1 mimetic peptide (PK22), targeting peptide-conjugated cytotoxic mertansine (RM) and photodynamic agents of DiIC18(5) (DiD). The counterpart biomimetic lipoprotein system without RM (termed

as BL-D) was fabricated as control. Both BL-D and BL-RD were nanometer-sized particles with a mean diameter of less than 30 nm and could be efficiently internalized by cancer cells. After intravenous injection, they can be specifically accumulated at tumor sites. When comparing to the counterpart BL-D, BL-RD displayed superior capability to permeate across the tumor mass, extravasate from tumor vasculature to distant regions and efficiently access the cancer cell fractions in a solid tumor, thus producing noticeable depression of the tumor growth. Taken together, BL-RD can be a promising delivery nanoplatform with prominent tumor-penetrating and cancer cells-accessing capability for effective tumor therapy.

1. Introduction

Compelling evidence has revealed that the nanosized vehicles are attractive approaches in cancer therapy because they can preferentially deliver a variety of therapeutic drug to tumor sites[1,2]. To date, a few liposomal formulations of doxorubicin (Doxil), irinotecan (Onivyde) and vincristine (Marqibo), polymeric micelles of paclitaxel (Genexol-PM) and albumin-bound paclitaxel (Abraxane) have been approved for cancer treatments[1,3]. However, these nanoformulations have only moderate enhancement of therapeutic benefits in the clinic[4]. The major issues are the limited drug penetration in tumor mass and their poor accessibility to cancer cell fractions in solid tumor[5−7]. In essence, cancer cells are heterogeneously distributed in tumor mass and account for only a small fraction of cell phenotypes in tumor biopsy[8]. At tumor sites, the disorganized tumor vascular network, extensively distributed stromal cells (e.g., tumor-associated macrophage, TAM; cancer-associated fibroblasts, CAF; etc.) and the dense physical barriers of extracellular matrix (ECM) comprise of the abominable obstacles hampering nano vehicles transport in a tumor[2,9,10]. Although the nano-sized particles can be specifically accumulated in tumor sites by exploiting the enhanced permeability and retention effects,[11−16]. they are extensively hijacked by stromal cells and barely accessed to the cancer cell fractions in a tumor[2,5,17−19]. A recent report reveals that only 0.7% of systemically administered nanoparticles can reach the tumor sites and less than 0.0014% of them are accessed by cancer cells[17]. Unarguably, the nano-formulations should be rationally designed to circumvent these dilemmas and improve the tumor-penetration and cancer cell-accessibility for effective tumor therapy.

The electron microscopy results have confirmed that the opening in tumor ECM barriers is generally less than 40 nm[20]. Lipoproteins, especially the high-density lipoprotein (HDL) and low-density lipoproteins, are natural endogenous nanoparticles with the mean diameter of 7−30 nm, potentiating it ideal nanoplatform to deliver various therapeutic agents to a tumor[20−24]. Increasing data have suggested that small-sized nanoparticles (less than 30 nm) could flexibly move to regions distant from the tumor vessels and penetrate into the deep interiors of tumor mass[2,25−27]. The small particle size of lipoproteins would facilitate their permeation in tumor mass, thereby providing an essential prerequisite to enhance their accessibility to cancer cells fractions in tumor. However, due to the heterogeneous distribution of cancer cells and various stromal cells in tumor, the accessing of lipoprotein-inspired nanoparticles to cancer cells fractions is

greatly challenged. Recent reports have revealed that the targeting RGD peptide modification in nanoparticles could be an effective method to enhance the recognition and internalization of nanoparticles by cancer cells[28,29]. In our previous results, we have also evidenced the crucial role of a CRGDfK peptide in enhancing the accessibility of wormlike micelles to cancer cell regions in tumor[30]. Rationally, a re-constructed lipoproteins system decorated with a CRGDfK peptide can be an encouraging nanoplatform with deep tumor-penetrating and cancer cells-accessing capability for effective antitumor therapy.

Herein, we designed a biomimetic lipoprotein-loading targeting peptide-conjugated cytotoxic mertansine (CRGDfK-S-S-Mer, shortened as RM) and photosensitizer DiD (termed as BL-RD) to improve their tumor penetration and cancer cells accessibility for combinational chemo-photodynamic therapy (Scheme 1). In the BL-RD system, the re-constructed lipoprotein-mimetic nanostructure with RM decoration would ameliorate their specific accumulation in tumor and facilitate their accessibility to cancer cells in vivo, while the lipophilic fluorescence dye of DiD was utilized for in vivo imaging and photodynamic therapy (PDT), ultimately benefiting the therapeutic outcomes in a synergistic manner. In a 4T1-induced breast cancer model, the specific tumor targeting, deep tumor penetration and cancer cells accessibility of BL-RD were gradually measured. Moreover, the in vivo antitumor effects were evaluated to verify their medical performance on tumor growth.

2. Materials and Methods

2.1. Materials

The 1,2-dioleoyl-sn-glycero-3-phosphocholine (DOPC) was supplied by Shanghai Advanced Vehicle Technology Pharmaceutical Ltd. (Shanghai, China). The apolipoprotein A1 (ApoA1)-mimetic peptide (PK22) and cyclic targeting peptide of CRGDfK were provided by GL Biochem (Shanghai) Ltd. (Shanghai, China). Mertansine was obtained from BrightGene BioMedical Technology Co., Ltd. (Jiangsu, China). DiD was purchased by Amyjet Scientific Inc. (Wuhan, China).

2.2. Cell lines and animals

The murine mammary 4T1 cancer cells, human MCF-7 breast cancer cells and murine NIH-3T3 embryonic fibroblast cells were supported by Cell Bank of Shanghai, Chinese Academy of
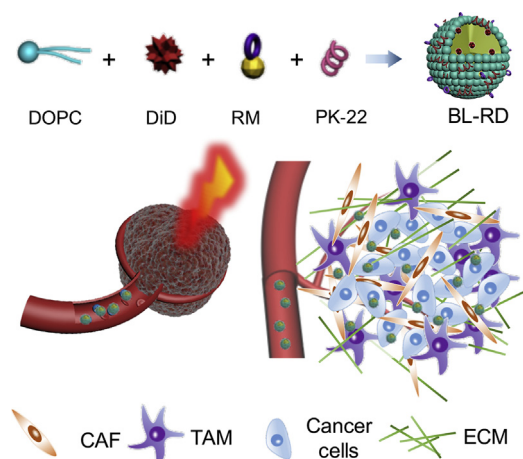
Scheme 1 Schematic illustration of CRGDfK-peptide-decorated biomimetic lipoprotein of BL-RD with efficient tumor-penetrating and cancer-cell-accessing capacity for anticancer therapy. BL-RD is an encouraging nanoplatform loading peptide-conjugated prodrug of RM and photosensitizer DiD for effective chemo-photodynamic therapy of breast cancer. (BL-RD, targeting peptide decorated biomimetic lipoprotein system; CAF, cancer-associated fibroblasts; DiD, DiIC18(5); DOPC, 1,2-dioleoyl-*sn*-glycero-3-phosphocholine; ECM, extracellular matrix; RM, targeting peptide-conjugated cytotoxic mertansine; TAM, tumor-associated macrophage).

Science (CAS, Shanghai, China). The 4T1 cancer cells with stable expression of green fluorescence protein (4T1-GFP) were provided by PerkinElmer Inc. (USA). The cancer cells were cultured in RPMI-1640 media supplemented with 10% fetal bovine serum (FBS, Gibco), and 100 U/mL of penicillin, and 100 μg/mL of streptomycin at 37 °C in a humidified incubator containing 5% CO_2. The NIH-3T3 cells were maintained in the Dulbecco's modified Eagle's medium (DMEM) media with similar supplements and cultured as described above.

Female nude mice (18−22 g) were provided by Shanghai Experimental Animal Center, CAS (Shanghai, China). All animal experiments were performed according to the experimental guidelines approved by the Institutional Animal Care and Use Committee (IACUC) of Shanghai Institute of Materia Medical (SIMM), CAS, China.

2.3. Synthesis of targeting peptide conjugated prodrug of RM

The synthesis procedure of RM was listed in Supporting Information Fig. S1. In brief, mertansine and 2,2′-dithiodipyridine (molar ratio of 1:1.2) were dissolved in 2 mL methanol, and 10 μL trimethylamine was dropped into the mixed solution under stirring. The mixture was kept at room temperature for 24 h and collected to purify the intermediate product of Mer-S. Then, Mer-S and the cyclic CRGDfK peptide (molar ratio of 1.2:1) were dissolved in 2mL dimethyl sulfoxide (DMSO), followed by stirring at room temperature for further 24 h. The product of RM in the mixed solution was purified using the preparative reversed-phase high-performance liquid chromatography (HPLC) equipped with a Waters XBridge® Prep C18 column (5 μm, 250 mm × 19 mm) with the flow rate of 10.0 mL/min and detection wavelength of 254 nm. The mobile phase was acetonitrile (A)−water (B) in a gradient-dilution

method: 0−1 min, 10% A; 1−15 min, from 10% A to 90% A; 15−18 min, 90% A to 10% A; 18−20 min 10% A. The collected solution was lyophilized to obtain the RM conjugates and determined by mass spectrometry and nuclear magnetic resonance hydrogen spectroscopy.

2.4. Preparation and characterization of BL-D and BL-RD

BL-RD was composed of DOPC, DiD, RM and ApoA1-mimetic peptide of PK22 (weight ratio, 10:0.5:0.2:2). The ingredients of DOPC, DiD and RM were dissolved in mixed solution of chloroform/methanol ($v/v = 1:1$) in a round flask, evaporated to form a thin film and then dispersed in water. Thereafter, the mixed suspension was sonicated with a probe in ice-bath for 1.5 min to make a liposomal formulation (termed as Lipo-RD). The PK22 solution was dropped into the Lipo-RD and performed three heating (50 °C) and cooling (ice-cooled water) cycles to develop the BL-RD. By contrast, the counterpart formulation of BL-D that consisted of DOPC, DiD and PK22 was prepared in the same procedure. The morphologies of BL-RD and BL-D were determined by transmission electronic microscope (TEM, Tecnai G2 F20 S-Twin, FEI) measurements after negative staining with uranyl acetate and the typical images were analyzed to calculate the mean diameters. Due to the interference of DiD in these formulations, the particle size distribution of these nano-formulations cannot be measured by dynamic light scattering method.

The drug-loading capacity and EE values of DiD and RM in the biomimetic lipoprotein system were respectively determined. The free DiD or RM in these nanoformulations were separated by ultra-filtration method. The amount of DiD in these nanoformulations was determined using fluorescence spectrum analysis (Enspire, Perkin−Elmer, Singapore). Meanwhile, the drug amount of RM in BL-RD was analyzed using a HPLC (Waters Alliance, USA) method as described above. The content of PK22 in BL-RD and BL-D were quantified using an ultraviolet−visible spectrum analysis. The drug-loading capacity was calculated as the weight percentage of the encapsulated drug to the total amount of all ingredients in the nano-formulation. The encapsulation efficiency (EE) was determined as the ratio between the amount of encapsulated drug compared to the total drug amount in the nanoformulation. The measurements were performed in triplicate.

To determine their stability in physiological fluids, BL-D and BL-RD were respectively diluted in phosphate buffered solution (PBS) at pH 7.4 and PBS (pH 7.4) containing 10% FBS, and incubated for 24 h. At 2, 8 and 24 h of incubation, samples were separated by ultra-filtration method. All samples are in triplicate. The DiD entrapped in BL-D or BL-RD was analyzed with fluorescence spectrum analysis while the RM amount that encapsulated in BL-RD was determined with the aforementioned HPLC method.

To determine the responsiveness of RM to intracellular reducible environments, RM were incubated in PBS with 1×10^{-5} or 1×10^{-2} mol/L glutathione (GSH) for 2 h. Then, the mixed solution was analyzed by the aforementioned HPLC method to characterize the typical peaks of RM and the degraded product of mertansine. Then, to evaluate the impact of laser irradiation on the degradation of RM in BL-RD, BL-RD were incubated in PBS with laser, PBS with 1×10^{-2} mol/L GSH, PBS with 1×10^{-2} mol/L GSH with laser (at 5 μg/mL of RM). For laser-irradiated groups, samples were irradiated at a density of

2 W/cm^2 for 5 min, and then incubated at 37 °C for 2 h. At certain time intervals, samples were analyzed using the HPLC method as described above to determine the degradation of RM into mertansine upon these incubation conditions. All the measurements were performed in triplicate.

The production of reactive oxygen species (ROS) from BL-D and BL-RD upon their exposure to 655 nm laser was monitored using the singlet oxygen sensor green (SOSG, Thermo Fisher) as a fluorescence probe. In brief, 200 μL of water, free DiD, BL-D and BL-RD at 0.5 μg/mL of DiD containing 10 μmol/L SOSG was irradiated with 655 nm laser for 8 min at a power density of 2 W/cm^2. At predetermined time points, the fluorescence intensity of the samples was recorded using the microplate reader (Enspire, Perkin−Elmer, Singapore). All the measurements were performed in triplicate.

2.5. Cellular uptake

The cellular uptake of BL-D and BL-RD was measured under confocal laser scanning microscopy (CLSM, TCS-SP8 STED, Leica, Solms, Germany) and further quantified by flow cytometer analysis (FACSCalibur system, BD, New York, USA). The fluorescence dye DiD was used as an imaging probe for the detections. For CLSM measurements, 4T1 cancer cells were seeded on a round coverslip (14 mm in diameter) in 24-well plate at a density of 5×10^4 cells/well and incubated overnight. Then, free DiD solution, BL-D and BL-RD were added to each well at 0.25 μg/mL of DiD and incubated for 4 h. After that, the cells were stained with LysoTracker Green DND-26 (Molecular Probe, USA) and Hoechst 33342 (blue, Beyotime) for visualization under CLSM. BL-D and BL-RD were donated as red fluorescence signals in the captured pictures. All samples are in triplicate.

For quantification, BL-D and BL-RD was added to the 24-well plate at 0.25 μg/mL of DiD and incubated for 4 h at 37 °C. Afterward, these cells were collected and the fluorescence intensity in each sample was determined by flow cytometer analysis (FACSCalibur system, BD, New York, USA). The 4T1 cells without any treatment were performed as negative control. All the experiments were performed in triplicate. The cellular uptake of BL-D and BL-RD was also measured in MCF-7 breast cancer cells. All the measurements were performed in triplicate.

To investigate the possible mechanism of the preferential uptake of BL-RD over BL-D, the expression of the specific receptors of scavenge receptor class B type 1(SR-BI) and $\alpha_v\beta_3$ integrin were determined in 4T1 cancer cells and normal NIH-3T3 cells. To test the expression of SR-BI, cells were successively stained with primary anti-SR-BI antibody (ab217318, Abcam) and followed with secondary antibody of Cy3-labeled IgG (H+L) (Beyotime) for the flow cytometer analysis. Likewise, to determine the $\alpha_v\beta_3$ integrin expression, cells were stained with primary anti-$\alpha_v\beta_3$ integrin antibody (sc-7312, SantaCruz, USA) and followed with secondary antibody of Alexa Fluor 488 labeled IgG (H+L) (Yeasen) for flow cytometer analysis. Meanwhile, the expression of SR-BI and $\alpha_v\beta_3$ integrin was also evaluated in 4T1-induced tumor by CLSM. To clarify the role of SR-BI and $\alpha_v\beta_3$ integrin in the cellular uptake of BL-RD, the 4T1 cells were pretreated with PK22 and CRGDfK peptide or their combination at 70 μmol/L for 60 min, and then incubated with BL-RD at 0.25 μg/mL DiD for 4 h. Afterward, cells were collected and measured by flow cytometer analysis. Cells without any treatment were performed as the negative control. All the experiments were performed in triplicate.

2.6. Photodynamic activities of BL-RD in 4T1 cancer cells

To evaluate the photodynamic activity of BL-RD in 4T1 cancer cells, 5×10^4 4T1 cells were seeded in 24 well plates with a round coverslip in each well and incubated overnight. The 4T1 cells were treated with PBS, free DiD, RM, BL-D and BL-RD at 0.25 μg/mL of DiD or 0.1 μg/mL of RM, respectively, and incubated at 37 °C for 4 h. Then, cells were washed twice and cultured in fresh culture media with Hoechst 33342 (100×, Beyotime, China) and fluorescence probe 2′,7′-dichlorodihydrofluorescein diacetate (DCFH-DA, 10 μmol/L, Sigma) for 20 min. Cells treated with PBS, free DiD, BL-D and BL-RD were exposed to 655 nm laser at 2 W/cm^2 for 2 min, and visualized under CLSM (TCS-SP8 STED, Leica, Germany). By contrast, cells treated with PBS, RM, BL-RD without laser irradiation were performed as a control. All the measurements were performed in triplicate.

2.7. Cytotoxicity

The cytotoxicity of RM, BL-D, BL-RD and the counterpart biomimetic lipoprotein-loading DiD and mertansine (termed as BL-MD) was measured in murine 4T1 cancer cells and human MCF-7 cancer cells. In brief, cells were seeded into 96 well plates at 3×10^3 cells per well, and cultured overnight. BL-D, RM, BL-MD and BL-RD were respectively added to each well with the RM concentrations ranging from 0.0022 to 6.78 μmol/L and DiD concentrations within 0.0042 and 13.02 μmol/L. After 48 h of incubation, the cell viability in each group was determined by thiazolyl blue tetrazolium bromide (MTT, Sigma) assays. All samples are in triplicate.

The therapeutic effects of BL-D-mediated photodynamic activity were measured in 4T1 cells by cell apoptosis assays. In brief, 4T1 cells were seeded in 24 well plates at 5×10^4 cells per well and cultured overnight, and then incubated with BL-D at 0.26 μmol/L DiD for 24 h. Then, cells were harvested, washed twice with PBS, and exposed to 655 nm laser for 5 min at 0, 0.5, 1 and 2 W/cm^2. Afterwards, cells were stained with the apoptosis detection kit and measured by flow cytometer analysis. All samples are in triplicate.

To evaluate the combinational chemo-photodynamic therapy of BL-RD on cancer cells, 4T1 and MCF-7 cells were seeded in 96 well plates at 3×10^3 cells per well, and cultured overnight. Cells were treated with PBS, free DiD, BL-D, BL-MD and BL-RD at 0.26 μmol/L of DiD for 4 h, respectively, and replaced with fresh culture media. Then, these cells were exposed to 655 nm laser at 0, 0.5, 1.0 and 2.0 W/cm^2 for 2 min. Afterward, cells were cultured in fresh culture media containing free DiD, BL-D, BL-MD and BL-RD at 0.26 μmol/L of DiD. After 48 h, the cell viability was determined by MTT assays. The PBS-treated group without laser irradiation was performed as a control. All the measurements were performed in triplicate.

The apoptosis induced by BL-RD-mediated combinational therapy were evaluated in 4T1 cancer cells. Cells seeded in 24 well plates were treated with PBS, PBS+laser, free DiD+laser, RM, BL-D+laser, BL-RD and BL-RD+laser at 0.26 μmol/L of DiD and 0.14 μmol/L of RM for 24 h, respectively. Then, cells were harvested, washed twice with PBS for further measurements. For laser-irradiated groups, cells were exposed to a 655 nm laser at 2.0 W/cm^2 for 5 min. Afterwards, cells were stained with the apoptosis detection kit for flow cytometer analysis. All the measurements were performed in triplicate.

2.8. Penetration of BL-RD in multicellular spheroids

A 3D multicellular spheroids (MCS) was established from 4T1 cells as an *in vitro* model to evaluate the penetrating ability of BL-RD. In brief, 1.0 wt% agarose was added into 48 well plate (200 μL per well). Then, the 4T1 cells were seeded on the plate at a density of 1×10^3 per well and incubated at 37 °C for 4 days to form MCS model. When the MCS volume reached 200−300 μm in diameter, free DiD, BL-D and BL-RD were added to the 48-well plate at 0.5 μg/mL of DiD and incubated for 4 h at 37 °C. Then, these spheroids were collected, washed with PBS and visualized under CLSM (TCS-SP8 STED, Leica, Germany).

2.9. In vivo tumor accumulation of BL-RD

The accumulation of BL-RD at tumor sites was determined in a 4T1-induced breast cancer model, which was developed by subcutaneous injection of 1×10^6 4T1 cells on the right second mammary gland. When the tumor volume reached 150 mm^3, the tumor-bearing mice were respectively injected with free DiD, Lipo-RD, BL-D and BL-RD at a DiD dose of 5 mg/kg. DiD was used as the fluorescence probe for *in vivo* imaging detections. At predetermined time points, mice were anaesthetized and the fluorescence signals of DiD from these groups were collected using the *in vivo* imaging system (IVIS Spectrum, Perkin−Elmer). At 12 h postinjection, mice were autopsied, and the major organs including heart, liver, spleen, lung, kidney, and tumor were carefully collected for imaging under the *in vivo* imaging system. Then, these organs were weighed and homogenized. The fluorescence intensity of DiD in these homogenates were examined using a microplate reader (Enspire, Perkin−Elmer, Singapore).

2.10. Tumor penetration of BL-RD

The tumor-bearing mice were respectively injected with free DiD, BL-D and BL-RD at a DiD dose of 5 mg/kg. The *in vivo* permeation of BL-RD in tumor sites was firstly determined by photoacoustic imaging. DiD was used as *in vivo* photoacoustic imaging probe. At 12 h postinjection, the photoacoustic signals from each group were monitored using the photoacoustic imaging system (Vevo 2100 LAZR, VisualSonic FUJIFILM). The photoacoustic signals of free DiD, BL-D and BL-RD were denoted as green signals in the captured images, and the ultrasound signals of the tumor tissues were collected to obtain the anatomical images.

Then, the permeation of BL-RD in tumor mass was further measured. The tumor tissues from free DiD-, BL-D-, Lipo-RD- and BL-RD-treated groups were collected at 12 h after injection. These tumor tissues were embedded in optimal cutting temperature compound (SAKURA, USA), frozen at −20 °C for cryostat section at 10 μm (Leica CM 1950, Germany). These tumor sections were fixed with 4% paraformaldehyde, and then stained with 4′,6-diamidino-2-phenylindole (DAPI, blue, Sigma) and phalloidin-FITC (green, Beyotime) for visualization under CLSM (TCS-SP8 STED, Leica, Germany). The fluorescence signals in the whole tumor mass were collected to provide a full view of the tumor mass. The fluorescence signals of DiD from each treatment was analyzed using the Image J software (National Institutes of Health, Bethesda, USA).

Meanwhile, to evaluate the extravasation of BL-RD from tumor vasculature, these tumor sections were fixed with 4% paraformaldehyde, incubated with primary monoclonal antibody against CD31 (anti-CD31, Abcam, ab7388) overnight at 4 °C, and then stained with FITC-conjugated secondary antibody (Beyotime, Jiangsu, China) and DAPI (Beyotime, Jiangsu, China) for visualization. BL-D and BL-RD were denoted as red signals in the captured images. The extravasation of BL-D and BL-RD from tumor vessels were assessed as the distance of the red signals away from the tumor vasculature. Afterwards, a 2.5D view of the extravasation profiles was analyzed using the Image J software.

2.11. In vivo accessing of BL-RD to cancer cells

The tumor mass comprised of a large number of stromal cells and a small fraction of tumor cells in tumor biopsy. TAM, CAF, and EC are the major components of stromal cells[10]. To evaluate the internalization of BL-RD by these stromal cells under CLSM, they were marked with specific antibodies to distinguish them in tumor sections respectively. To determine their uptake by TAM in a tumor, the tumor sections were incubated with a primary monoclonal antibody against F4/80 (Abcam, ab6640) and Alexa Fluor 488 labeled secondary antibody (Yeasen, China) to outline the profiles of TAM. The cellular uptake of BL-D and BL-RD could be defined as the colocalization of the red signals from BL-D or BL-RD and the green signals of TAM. Similarly, the tumor sections were simultaneously labeled with the specific primary monoclonal antibodies against α-smooth muscle actin (α-SMA, Abcam, ab5694) and CD31 (Abcam, ab7388), and then incubated with the Alexa Fluor 488-labeled secondary antibody (Yeasen, China) and Cy3-labeled secondary antibody (Beyotime, Jiangsu, China), respectively. In the captured images under CLSM, CAF was defined as the α-SMA$^+$/CD31$^-$ cells which were expressed as cells with green signals (α-SMA) excluding those with white signals (CD31), while EC was presented as the cells with white signals of CD31. By contrast, the tumor sections were stained with DAPI for visualization under CLSM (TCS-SP8 STED, Leica, Germany). The internalization of BL-D or BL-RD by these stromal cells could be identified as the merging of red signals with the specific markers of different stromal cells.

To investigate the accessing of BL-RD to cancer cells in tumor, the tumor model was induced by subcutaneous injection of 1×10^6 4T1-GFP cancer cells. When the tumor size reached about 150 mm^3, the tumor bearing mice were intravenously administered with free DiD, BL-D, Lipo-RD and BL-RD *via* a tail vein. At 12 h after injection, the tumor tissues were collected, sectioned and stained with DAPI for observations. The 4T1-GFP cancer cells in tumor were expressed as cells with green fluorescence signals in the captured images. The accessing of BL-RD, and BL-D to cancer cells was denoted as the colocalization of red signals with green signals of 4T1-GFP cancer cells. Afterwards, the accessing of nanoformulations to 4T1-GFP cancer cell regions in tumor tissues were analyzed using the Image J software.

2.12. In vivo photodynamic activity of BL-RD in tumor

The *in vivo* photodynamic activity of BL-RD in tumor was measured in the 4T1-induced tumor model. The tumor-bearing mice were treated with PBS, PBS+laser, RM, BL-RD, free DiD+laser, BL-D+laser, BL-RD+laser at 5 mg/kg of DiD or 2 mg/kg of RM *via* tail injection, respectively. For laser-irradiated groups, at 12 h postinjection, DCFH-DA was intratumorally injected to the tumor tissues at 2.0 mg/kg. Twenty minutes later,

the tumor sites were exposed to 655 nm laser at 2.0 W/cm^2 for 2 min. Then, mice were sacrificed and the tumors were collected, sectioned and stained with DAPI for observations under CLSM. The production of ROS was exhibited as green signals in the captured images.

2.13. In vivo therapeutic effects of BL-RD-mediated chemo-photodynamic therapy on tumor growth

The *in vivo* therapeutic effects of BL-RD on tumor growth was measured in 4T1-induced tumor model by subcutaneous injection of 4T1 cells at 1×10^6 per mouse. When the tumor volume reached around 150 mm^3, mice were randomly divided into 7 groups ($n=5$) and treated with PBS, PBS+laser, RM, BL-RD, free DiD+laser, BL-D+laser, BL-RD+laser at 5 mg/kg of DiD or 2 mg/kg of RM *via* tail injection, respectively. For laser-irradiated groups, the tumor sites were exposed to 655 nm laser at 2.0 W/cm^2 for 2 min at 12 h after injection. The treatments were repeated every four days (day 1, 5 and 9) for a total of three times (Fig. 9A). The body weight and tumor volume were monitored at certain time intervals. The width and length of the tumor were measured using a digital caliper to calculate the tumor volume. The tumor growth index (TGI) of each treatment was calculated as the tumor volume at certain time points compared to that at the initial time of drug administration. At day 18 after the first treatment, the tumor size was measured and the TGI values from each treatment were calculated. The tumor tissues from each group were carefully collected, photographed and weighed to calculate the inhibitory effects on tumor growth. Then, the tumor tissues from each group were fixed in 4% formalin solution, embedded in paraffin, sectioned at 5 μm for histological examinations by H&E staining method. To detect the proliferation of cancer cells in a tumor, the tumor sections were stained with anti-Ki67 antibody (GB13030-2, Servicebio, China) for immunohisto-chemistry examinations.

2.14. Statistical analysis

Data were expressed as mean values±standard deviation (SD). The statistical analysis between two groups was determined by a two-tailed Student's *t*-test. The difference was considered as significant when the *P* value was less than 0.05.

3. Results and discussions

3.1. Preparation and characterization of BL-RD

Lipoproteins are usually composed of diverse proteins (*e.g.*, ApoA1) and lipids (*e.g.*, phospholipids and cholesterol esters), which can load a variety of therapeutic and imaging agents for tumor-targeted delivery[21,22,31]. ApoA1 is a major protein of HDL, and the amphiphilic ApoA1-mimic peptide can be used to interact with the phospholipid membranes to develop the biomimetic lipoprotein system[32,33]. Inspired by the components of natural HDL, BL-RD was fabricated from the synthetic phospholipids of DOPC, ApoA1-mimetic peptide of PK22 (sequence, PVLDLFRELLNELLEALKQKLK), targeting peptide-conjugated mertansine of RM and photosensitizers DiD. In the BL-RD system, DOPC and ApoA1-mimic peptide PK22 were

used as the major ingredients to construct the lipoprotein system. Mertansine was a highly cytotoxic agent that can efficiently disrupt the microtubule to inhibit cell proliferation and differentiation for anticancer therapy[34]. The cyclic CRGDfK peptide may specifically recognize highly expressed $\alpha_v\beta_{3/5}$ integrins in tumor vessels or cancer cells (*e.g.*, 4T1 breast cancer cell),[35−38]. which could be conjugated with cytotoxic mertansine *via* disulfide bonds to synthesize the amphiphilic peptide−drug conjugates of RM (Figs. S1 and S2). Meanwhile, the lipophilic fluorescence dye DiD could be used as an efficient photosensitizer to generate ROS upon laser irradiation for PDT. In this manuscript, both the peptide−drug conjugates RM and photosensitizer DiD can be loaded into the BL-RD system to realize their effective accessing to cancer cells in solid tumors for combinational chemo-photodynamic therapy. By contrast, the biomimetic-lipoprotein-loading DiD but without RM was prepared as control nanoparticles (termed as BL-D) to detect the impact of targeting peptide decoration on tumor penetration, cancer cell accessibility and therapeutic effects.

The amphiphilic RM can be flexibly incorporated into the reconstructed lipoproteins *via* hydrophobic interactions with the hydrophobic mertansine segments inside the nanovehicles and hydrophilic CRGDfK peptide on the surface,[24]. which was supposed to facilitate their permeation across the tumor mass and enhance their accessibility to cancer cells for cancer therapy. Meanwhile, DiD is a lipophilic-membrane-labeled fluorescence dye with the maximal absorption wavelength of 644 nm and a maximal emission wavelength of 665 nm,[39]. which can be loaded inside the reconstructed lipoproteins to potentiate its applications in fluorescence imaging, photoacoustic imaging, and PDT. The loading capacity of RM in BL-RD was 1.46±0.01% with the EE value of 92.14±0.72%. The calculated results showed the ratio of cyclic targeting peptide in BL-RD was 0.7% in weight. Meanwhile, the loading capacity of DiD in BL-RD and counterpart BL-D was 3.62±0.12% and 3.85±0.05% with the EE values of 91.55±3.22% and 96.03±1.23%, respectively. The content of PK-22 in BL-RD and BL-D was 14.77±0.11% and 15.27±0.19%, respectively. These measured results suggested that both RM and DiD could be highly entrapped in the BL-RD system, which can be used for combinational chemo-photodynamic therapy.

Then, the morphologies of BL-RD and counterpart BL-D were visualized under TEM, which showed both BL-RD and counterpart BL-D were nanometer-sized spherical particles. Due to the interference of DiD on the particle size measurements by dynamic light scattering, the mean diameter was evaluated by image analysis of the TEM images from three fields-of-views, which revealed that the mean diameter of BL-RD and counterpart BL-D were 22.07±4.31 and 21.36±4.96 nm, respectively (Fig. 1A and B). Compelling data have evidenced that small particles with the diameter less than 40 nm could be efficiently delivered to tumor sites and penetrate the tumor mass[2,25−27,40]. The small particle size of BL-RD and BL-D (less than 30 nm) could be beneficial for their specific accumulation and deep penetration in tumor tissues.

Moreover, to evaluate their stability in physiological fluids, both BL-RD and BL-D were mixed in PBS at pH 7.4 and PBS (pH 7.4) with 10% FBS for 24 h, respectively. After 24 h of incubation, the remained DiD in BL-RD and BL-D was over 88% in PBS and PBS+10% FBS, respectively (Fig. 1C and Supporting Information Fig. S3). Meanwhile, the RM that remained in BL-RD was more than 80% at 24 h of incubation in PBS (pH 7.4) and PBS+10% FBS
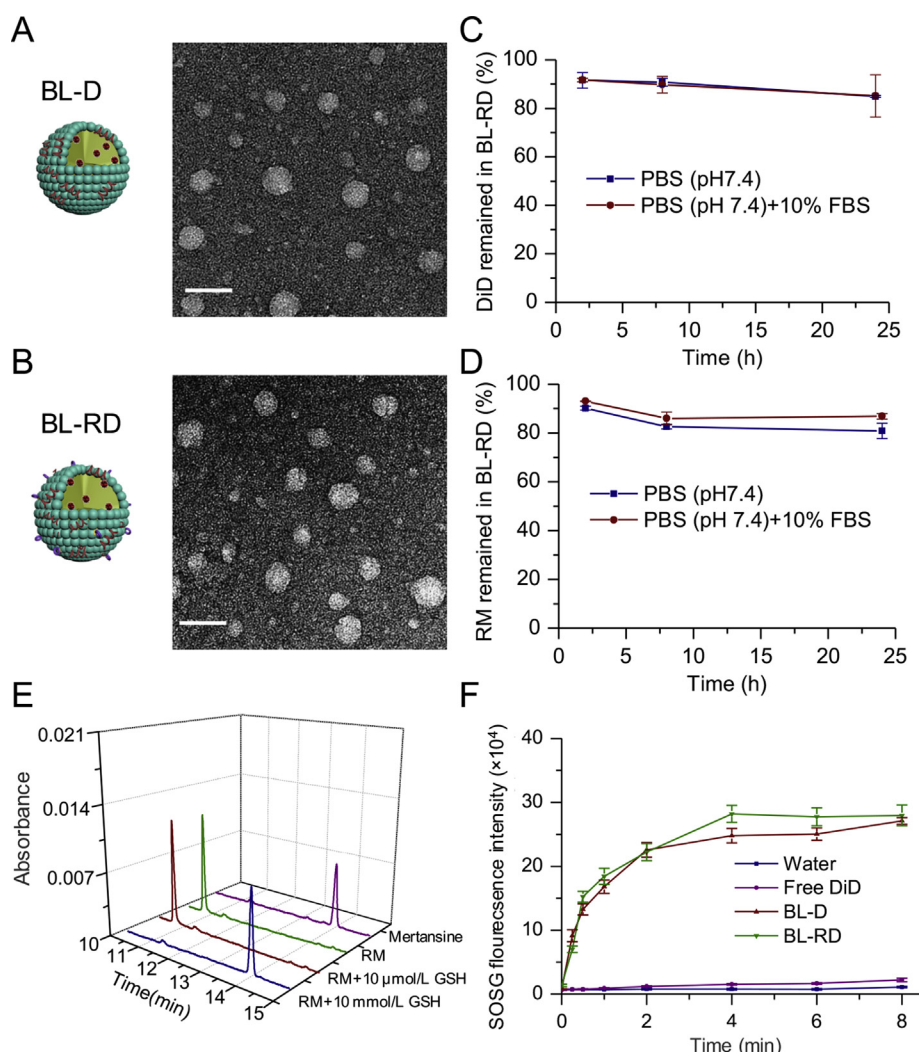
Figure 1 Characterization of BL-D and BL-RD. (A) Typical TEM images of BL-D, scale bar = 50 nm. (B) Typical TEM images of BL-RD, scale bar = 50 nm. (C) The percentage of DiD remained in BL-RD upon their incubation PBS (pH 7.4) and PBS (pH 7.4) with 10% FBS. Data are mean±SD ($n=3$). (D) The percentage of RM remained in BL-RD upon their incubation PBS (pH 7.4) and PBS (pH 7.4) with 10% FBS. Data are mean±SD ($n=3$). (E) The responsiveness of RM to GSH at 1×10^{-5} and 1×10^{-2} mol/L. (F) The production of ROS from BL-D and BL-RD upon their exposure to 655 nm laser. Data are mean±SD ($n=3$).

(Fig. 1D) , respectively. These results indicated the good stability of BL-D and BL-RD in the mimicked physiological fluids. In addition, given the high GSH level ($2-1\times10^{-2}$ mol/L) in cytoplasm, the degradation of RM was measured in PBS with 1×10^{-5} or 1×10^{-2} mol/L GSH (Fig. 1E). The measured results indicated that RM was rarely changed in PBS at 1×10^{-5} mol/L of GSH but completely degraded into cytotoxic mertansine at 1×10^{-2} mol/L of GSH within 2 h, validating the intelligent responsiveness of RM to the intracellular reducible environments. The good stability of BL-RD in physiological fluids and the bioreducible properties of RM in BL-RD could be beneficial for their tumor accumulation and achievement of antitumor effects.

To measure the photodynamic activity of BL-D and BL-RD, free DiD, BL-D and BL-RD were incubated with the SOSG regent and exposed to 655 nm laser irradiation, respectively. The production of ROS was monitored by fluorescence analysis at predetermined time points (Fig. 1F). In free DiD group at 0.5 μg/mL, the production of ROS was negligibly detected. Interestingly, when DiD was encapsulated into the biomimetic lipoproteins,

both BL-RD and BL-D produced a large amount of ROS upon laser irradiation, which was remarkably higher than that of free DiD. The photosensitizer of DiD could be activated to produce ROS upon their exposure to 655 nm laser[41]. However, the absorption of DiD at 655 nm is much lower in PBS due to its high lipophilicity but remarkably enhanced after their incorporation into the nanosystem of BL-D and BL-RD, which would be responsible for the higher ROS production of BL-RD and BL-D *versus* free DiD (Supporting Information Fig. S4). The effective production of ROS from BL-RD and BL-D upon laser irradiation provide an essential prerequisite for PDT[42].

Also, to some extent, the produced ROS by photosensitizer DiD might reduce the GSH levels in cancer cells, which might impact the reducible sensitivity of RM in BL-RD. To clarify this hypothesis, the degradation of RM in BL-RD was measured in PBS with laser, PBS with 1×10^{-2} mol/L GSH, PBS with 1×10^{-2} mol/L GSH and laser irradiation. As shown in Supporting Information Fig. S5, the RM degradation was rarely detected in BL-RD with laser irradiation (Fig. S5A), but rapidly completed
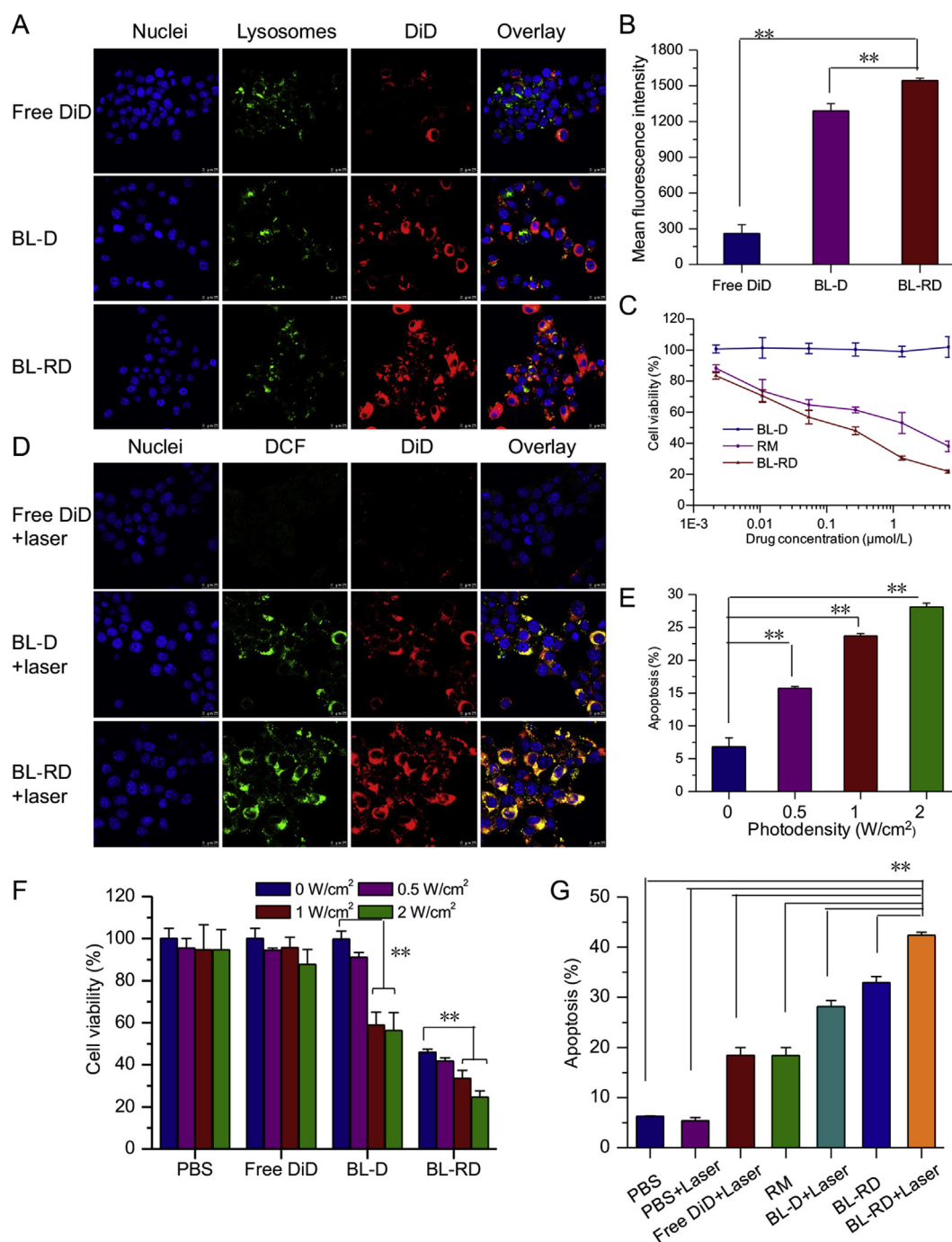
Figure 2 The *in vitro* cellular uptake and therapeutic effects of BL-RD in 4T1 cancer cells. (A) Cellular uptake of BL-D and BL-RD in 4T1 cells determined by CLSM, scale bar=25 μm. (B) Quantified cellular uptake of BL-D and BL-RD in 4T1 cancer cells by flow cytometer analysis. Data are mean±SD (*n*=3). **P<0.01. (C) Cytotoxicity of BL-D and BL-RD in 4T1 cancer cells. Data are mean±SD (*n*=3). (D) Production of ROS in 4T1 cancer cells treated with free DiD, BL-D and BL-RD upon their exposure to 655 nm laser at a power density of 2.0 W/cm² for 2 min, scale bar=25 μm. DCFH-DA was used as probe to monitor the production of ROS in 4T1 cancer cells. (E) BL-D induced apoptosis in 4T1 cells upon their exposure to laser irradiation at different density. Data are mean±SD (*n*=3). **P<0.01. (F) The therapeutic effects of BL-RD mediated chemo-photodynamic combinational therapy in 4T1 cancer cells. Data are mean±SD (*n*=3). **P<0.01. (G) The apoptosis in 4T1 cancer cells induced by BL-RD mediated chemo-photodynamic combinational therapy. Data are mean±SD (*n*=3). **P<0.01.

within 30 min when BL-RD was incubated with GSH (1×10^{-2} mol/L, Fig. S5B). When BL-RD with GSH (1×10^{-2} mol/L) was exposed to laser irradiation, the RM

degradation was reduced within 30 min but could be accomplished at 2 h of incubation (Fig. S5C). These results confirmed the sensitivity of RM in BL-RD to the high reducible environments in
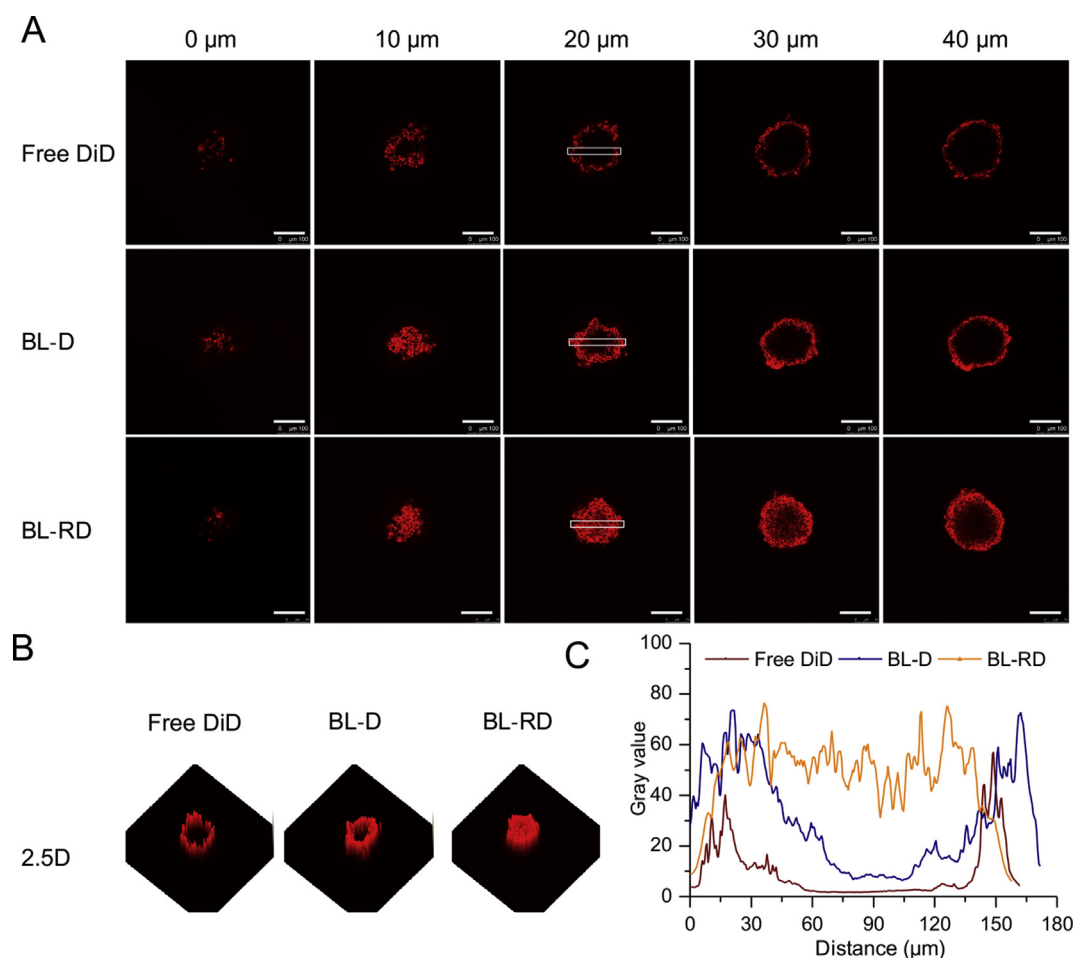
Figure 3 The *in vitro* tumor penetration of BL-RD in 4T1-induced MCS. (A) The *in vitro* imaging of free DiD, BL-D and BL-RD in MCS at certain distance intervals, scale bar = 100 μm. (B) The 2.5D imaging of free DiD, BL-D and BL-RD in MCS. (C) The quantified diffusion of BL-D and BL-RD in while rectangle regions of MCS by Image J software.

cytoplasm, which would be necessary to achieve the pharmacological activities after their uptake by cancer cells.

3.2. In vitro cellular uptake and therapeutic effects of BL-RD

The cellular uptake of BL-RD and BL-D were determined in 4T1 cancer cells using CLSM and flow cytometer analysis, wherein DiD was used as a fluorescence dye for the measurements. The captured images showed that both BL-RD and BL-D could be extensively internalized into 4T1 cancer cells (Fig. 2A). The flow cytometer results showed that the cellular uptake of BL-RD was significantly higher than that of BL-D in 4T1 cancer cells (Fig. 2B). Meanwhile, the enhanced cellular uptake of BL-RD over BL-D was also confirmed in MCF-7 cells (Supporting Information Fig. S6). Compelling evidence also revealed that the reconstructed lipoproteins could be efficiently internalized by a variety of cancer cells from murine or human[31−33]. The ApoA1 is a major protein of HDL, which would preferentially bind to the specific receptors of SR-BI. In the BL-RD system, the ApoA1 mimic peptide would facilitate its interactions with the SR-BI receptors and the cyclic CRGDfK peptide would promote its binding to the $\alpha_v\beta_3$ integrins on cancer cells, thereby enhancing their internalization by cancer cells. To illustrate the possible mechanism of the

enhanced uptake of BL-RD *versus* BL-D, the expressions of SR-BI and the $\alpha_v\beta_{3/5}$ integrins receptors were measured, which revealed that both SR-BI and $\alpha_v\beta_3$ integrins were highly expressed on 4T1 cancer cells and 4T1-induced tumors (Supporting Information Figs. S7 and S8). When the 4T1 cells were pretreated with free ApoA1-mimic peptide, CRGDfK peptide or their combinations, the cellular uptake of BL-RD were drastically reduced, suggesting the important role of SR-BI and $\alpha_v\beta_{3/5}$ integrins in the preferential uptake of BL-RD in 4T1 cancer cells (Supporting Information Fig. S9).

Then, the cytotoxicity of BL-RD was measured in 4T1 and MCF-7 cancer cells, which was performed in comparison to the counterpart BL-D and biomimetic-lipoprotein-loading mertansine and DiD (BL-MD). The measured results indicated that all the mertansine-containing group of RM, BL-MD and BL-RM displayed notable inhibition of cell viability in a concentration-dependent manner, while the counterpart BL-D had no inhibitory effects on cell viability (Fig. 2C, Supporting Information Figs. S10A and S11A). The half-inhibitory concentration (IC_{50}) in 4T1 cancer cells was 0.155 μmol/L for BL-RD, which was 8.35-fold lower than RM (1.294 μmol/L) and 3.13-fold lower than BL-MD (0.485 μmol/L). The higher cytotoxicity of BL-RD over other groups was also verified in MCF-7 cancer cells. The enhanced therapeutic effects of BL-RD over BL-MD could be
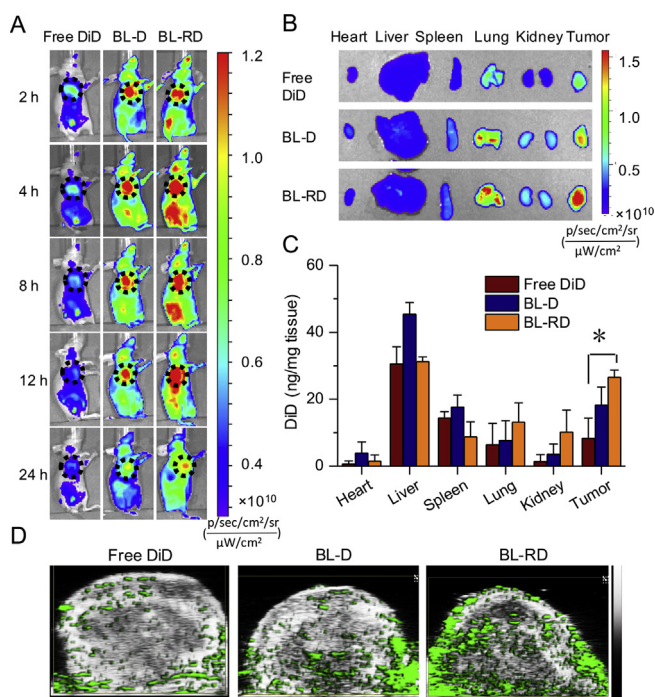
Figure 4 The *in vivo* tumor accumulation and permeation of BL-RD in 4T1-induced tumor model. (A) The *in vivo* imaging of free DiD, BL-D and BL-RD in tumor model at certain time intervals after intravenous injection. (B) The *ex vivo* imaging of free DiD, BL-D and BL-RD in major organs at 12 h postinjection. (C) Quantitative distribution of DiD from each group in various organs at 12 h post-injection. Data are mean±SD ($n=3$). $^*P<0.05$. (D) The tumor permeation of free DiD, BL-D and BL-RD examined by photoacoustic imaging at 12 h after injection, which was denoted as green signals in the captured images.

Figure 5 The permeation of BL-RD in tumor mass. (A) The intratumoral permeation of BL-D and BL-RD in the whole tumor mass measured by CLSM examinations. The tumor sections were stained with DAPI and Actin-Tracker green (phalloidin-FITC) for the observations, scale bar = 1 mm. (B) The quantified diffusion of BL-D and BL-RD in tumor mass from exterior to interior regions by Image J software.

mainly owing to the surface modification of targeting CRGDfK peptide.

Next, the production of ROS from BL-RD and BL-D in 4T1 cancer cells were determined at 4.0 h of incubation. The incubated 4T1 cells were stained with DCFH-DA and exposed to 655 nm laser at 2 W/cm^2 for 2 min. The production of ROS presented as green signals in the captured images. As shown in Fig. 2D, the green signals could be extensively observed in BL-RD-, and BL-D-treated groups with laser irradiations, which were colocalized with the red signals of biomimetic lipoproteins. However, no signal of ROS was detectable in BL-RD- and RM-treated 4T1 cancer cells without laser irradiation (Supporting Information Fig. S12). Thereafter, the 4T1 cancer cells were incubated with BL-D for 24 h and then exposed to laser irradiation at different power density (0, 0.5, 1.0, and 2.0 W/cm^2, Fig. 2E) to detect the therapeutic effects of BL-D-mediated photodynamic activity. Cells were stained with the apoptosis detection kit and quantified by flow cytometer analysis. The measured results showed that the percentage of cell apoptosis was increased with the density of laser irradiation, indicating the considerable photodynamic activities of BL-D and their potential antitumor effects.

Moreover, the combinational chemo-photodynamic therapy mediated by BL-RD were measured in 4T1 and MCF-7 cancer cells. Cells were treated with PBS, free DiD, BL-D and BL-RD, respectively. After 24 h of incubation, cells were cultured in fresh culture media and exposed to 655 nm laser at different power density (0, 0.5, 1.0, and 2.0 W/cm^2) and cells without any treatments were used as a negative control. When cells were not irradiated, only BL-RD showed considerable inhibition on cell viability but other samples of free DiD and BL-D had no cytotoxicity. When they were irradiated at 1.0 and 2.0 W/cm^2, both BL-D and BL-RD displayed obvious suppression of cell viability. The BL-D with 2.0 W/cm^2 of laser irradiation treatment resulted in a 56.32% inhibition of cell viability, suggesting the significant inhibitory effects of PDT alone. Of note, the BL-RD with 2.0 W/cm^2 of laser irradiation caused a 75.43% inhibition of cell viability, which was more effective than BL-D-mediated PDT, BL-RD-mediated chemotherapy and BL-MD-mediated chemo-photodynamic therapy (Fig. 2F and Fig. S10B). The combinational chemo-photodynamic therapeutic effects of BL-RD were also confirmed in MCF-7 cancer cells (Fig. S11B). Furthermore, the flow cytometer analysis revealed that BL-RD-mediated combinational therapy produced a 42.4% of cell apoptosis in 4T1 cancer cells, which was much higher than that of other groups (Fig. 2G). These experimental results effectively verified the
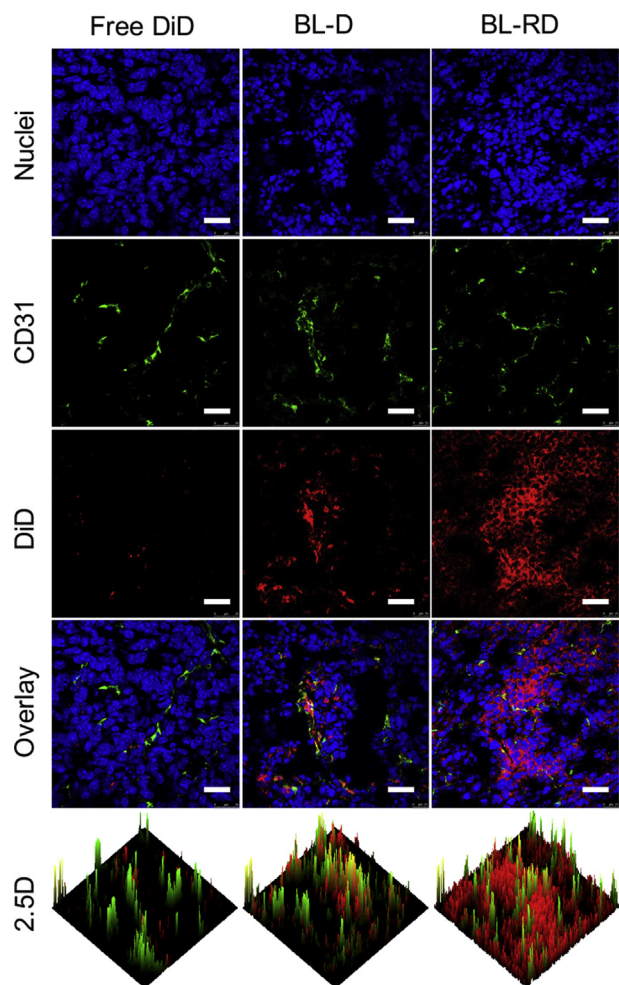
Figure 6 The extravasation of BL-D and BL-RD from tumor vasculature and their diffusion into distant regions away from the tumor vessels. The tumor vessels were marked with anti-CD31 antibodies and denoted as green fluorescence signals in CLSM images, scale bar = 25 μm. By contrast, the tumor sections were stained with DAPI for the visualization. A 2.5 D view profiles were provide using the Image J software.

notable therapeutic effects of BL-RD-mediated chemo-photodynamic therapy.

In addition, the penetrating capacity of BL-RD was evaluated in the MCS tumor sphere model, which was determined by CLSM at 4 h of incubation (Fig. 3). The intensity of DiD fluorescence signals in free DiD, BL-D and BL-RD was decreased with the Z-axis over 20 μm, but the fluorescence signals from BL-RD were much stronger than that from free DiD- and BL-D-treated groups (Fig. 3A). Meanwhile, a 2.5D view of their penetration profiles in tumor sphere model was provided to confirm the superior penetrating ability of BL-RD *versus* BL-D (Fig. 3B). The image analysis results suggested that the fluorescence signals of BL-RD could distribute throughout of the MCSs at 20 μm, but that of BL-D and free DiD were mainly located in the exterior regions of MCS (Fig. 3C). These *in vitro* results verified the effective penetrating capability of BL-RD in tumor sphere model, which could be mainly ascribed to the involvement of CRGDfK peptide in the re-constructed lipoprotein system.

3.3. In vivo specific tumor accumulation and penetration of BL-RD

The *in vivo* tumor accumulation and penetration of BL-RD was measured in 4T1-induced tumor model. By contrast, the counterpart BL-D- and liposomal-formulation-loading RM and DiD (Lipo-RD) were used for the measurements. At different time points after intravenous administration, the fluorescence signals of DiD from Lipo-RD-, BL-D- and BL-RD-treated mice were monitored using the *in vivo* Imaging system (Spectrum, Perkin—Elmer, USA). By contrast, free DiD-treated mice were performed as control. As shown in Fig. 4A, the fluorescence signals from BL-RD- and BL-D-treated mice could be detected at tumor sites at 2.0 h postinjection, and the fluorescence intensity maintained at a high level at different time points, suggesting their preferential accumulation at tumor sites. By contrast, the fluorescence signal from Lipo-RD-treated mice was peaked at 4 h and then gradually weakened thereafter (Supporting Information Fig. S13). The higher fluorescence intensity of BL-RD *versus* BL-D could be resulted from the prolonged blood circulation effect by the peptide modification in BL-RD[37]. At 12 h after injection, the major organs from each group were collected to record the fluorescence signals using the imaging system (Fig. 4B). Afterwards, these tissues were homogenized to quantify the distribution of DiD in these major organs (Fig. 4C and Supporting Information Fig. S14). The fluorescence intensity of BL-RD in tumor was 3.18-fold higher than that of free DiD, but only a slight but not significant increase was detected when comparing to the unmodified BL-D system. The particle size of nanoparticles was a major parameter affecting their accumulation in tumor tissues[43,44]. Both BL-RD and BL-D were small-sized particles with the mean diameter of 22.07±4.31 and 21.36±4.96 nm, respectively. The limited enhancement of BL-RD over BL-D in tumor accumulation could be attributed to their comparable particle size and bioinspired nanostructure of BL-RD and BL-D. However, in comparison to the liposomal formulation of Lipo-RD, the distribution of BL-RD in tumor was significantly improved 1.97-fold (Fig. S14). These results confirmed the efficient accumulation of BL-RD in tumor tissues and the significant enhancement of tumor accumulation over the liposomal formulations.

The deep tumor penetration in tumor mass is a crucial premise for effective chemotherapy or PDT-mediated antitumor treatments[34,45−47]. The penetration of BL-RD in tumor mass was firstly measured using the photoacoustic imaging system (Vevo LAZR, VisualSonic FujiFilm, Fig. 4D). DiD was used as the photoacoustic imaging agents owing to its maximal absorbance wavelength within the near infrared regions, represented by green signals in the captured images. By contrast, the ultrasound signals of the tumor mass were collected to obtain the anatomical images to determine their location in tumor. At 12 h after injection, mice were anesthetized and the photoacoustic signals of DiD at tumor sites from each group were documented. In Fig. 4D, the green signals of BL-RD and BL-D could be largely detected in the exterior and interior regions of tumor mass, suggesting their extensive intratumoral distribution. Moreover, the fluorescence intensity from BL-RD-treated group was stronger than that of BL-D group, especially in the inner sides of tumor mass, indicating the enhanced tumor permeation of BL-RD over counterpart BL-D.

Afterwards, the permeation of BL-RD in tumor mass was examined using CLSM. At 12 h postinjection, the tumor masses were collected and sectioned for CLSM measurements (Fig. 4
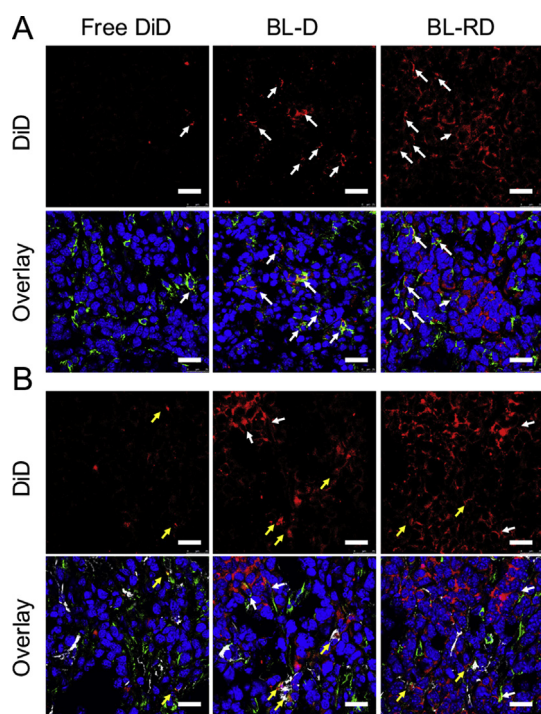
Figure 7 The internalization of BL-D and BL-RD by stromal cells of TAM, CAF and EC in tumor sites measured by LSCM, scale bar = 25 μm. (A) The internalization of free DiD, BL-D, and BL-RD by TAM in tumor, wherein TAM was donated as green fluorescence signals. The white arrows denoted as the co-localization of TAM with the red signals from the nanoparticles. (B) The internalization of BL-D and BL-RD by CAF and EC in tumor. In the captured images, CAF was denoted as α-SMA positive and CD31 negative (α-SMA$^+$/CD31$^-$) cells which was shown as green signals excluding white signals, while EC was presented as CD31 positive cells (white signals). The white arrows represented the localization of nanosystem in CAF while the yellow arrows referred to the localization of nanosystem in EC.

and Supporting Information Fig. S15). By contrast, the tumor sections were stained with actin-tracker Green (Beyotime, Jiangsu, China) and DAPI for the observations. In the captured images of the whole tumor mass, both BL-RD and BL-D were heterogeneously distributed in the whole tumor mass. The red fluorescence signals of Lipo-RD, BL-D and BL-RD could be readily detected wherever in the exterior regions or the deep inner sides of tumor mass, but that of free DiD was restricted in the edge of tumor tissues (Fig. 5 and Fig. S15). Of note, the image analysis data showed that the red signals of BL-RD in tumor mass could be more widely observed with stronger intensity than its counterparts BL-D and Lipo-RD. These results indicated that BL-RD, BL-D and Lipo-RD could permeate across the tumor mass and BL-RD displayed a more extensive permeation over BL-D and Lipo-RD with stronger intensity. Moreover, the extravasation of BL-RD from tumor vasculature was determined using CLSM. The tumor sections were stained with the specific makers of CD31 to outline the profiles of tumor vessels, and counterstained with DAPI to label the nuclei for clarification. As shown in Fig. 6, the red signals of DiD from BL-D-treated group were largely co-localized with those of CD31, indicating that the BL-D was mainly restricted in the tumor vasculature and entrapped in the perivascular area of the

tumors tissues. However, in BL-RD-treated group, the red signals could be detected with strong intensity at distant sites away from the tumor vessels, suggesting the efficient extravasation of BL-RD from the tumor vessels and their diffusion across the tumor matrix into distant regions. Although CRGDfK peptide in BL-RD can interact with endothelial cells in the tumor vessels, the synergistic combination of the small particle size and the HDL biomimetic properties in BL-RD could allow it transport across the leaky tumor vasculature and promote permeation to distant regions from the tumor vessels. The efficient permeation of BL-RD in the tumor mass and its flexible extravasation from the tumor vessels provided necessary premises to enhance its accessibility to the cancer cell fractions in the tumor.

As a result, the *in vivo* and *ex vivo* results revealed BL-RD could be specifically accumulated at the tumor sites and penetrate deeply into the interior regions of tumor mass, holding great premise to enhance their accessibility to cancer cells in solid tumors. The tumor accumulation of BL-RD was not significantly increased *versus* that of BL-D system, but was about 2-fold higher than that of liposomal formulation of Lipo-RD (Fig. 4C and Fig. S14). Both BL-RD and BL-D were nanometer-sized particles with the mean diameter less than 30 nm and the involved ApoA1-mimetic peptides could simulate the biological properties of HDL, which would be responsible for their efficient accumulation in solid tumors. Moreover, previous results have evidenced the outstanding advantages of small-sized particles in deep tumor penetration[2,26,44,48]. Due to the anomalous tumor vessels, elevated interstitial fluid pressure, widely existed stromal cells and dense ECM in tumor tissues[49−51], the permeation of nanoparticles in tumor mass was largely hampered. In particular, the opening in ECM was around 40 nm[20], which could permit the convective diffusion of small nanoparticles less than 40 nm in tumor. The small particle size of BL-RD and BL-D (less than 30 nm) could promote their diffusive transport across the tumor tissues. Notably, when comparing to the counterpart BL-D, BL-RD could be more effectively delivered to the interior regions of tumor, permeated across the tumor mass and extravasated from tumor vasculature into distant perivascular regions of tumor tissues. By comparing the components of BL-RD and BL-D, the cyclic CRGDfK peptide in BL-RD would be an essential factor accounting for the efficient extravasation and intratumoral diffusion. The deep tumor penetration and flexible diffusion of BL-RD in tumor mass provided an opportunity to facilitate their accessibility to cancer cells in tumor mass to exert the anti-tumor efficacy.

3.4. In vivo accessibility of BL-RD to cancer cells

The accessibility of nanoparticles to cancer cells in tumor mass is an essential prerequisite for their antitumor performance[48,52,53]. Cancer cells are co-evolved with diverse stromal cells (*e.g.*, TAM, CAF, and EC) to promote their outgrowth[10], but the delivery of nanoparticles to cancer cell fractions in solid tumor were largely hindered by the extensively existed stromal cells and the dense physical barriers of ECM. In view of the deep tumor penetrating ability of BL-RD and their flexible diffusion in tumor mass, the accessing to the heterogeneously distributed cancer cells in solid tumor could be reasonably enhanced. The cellular uptake of BL-RD by the stromal cells of CAF, TAM, EC and cancer cells in the tumor mass were determined, respectively. The tumor sections
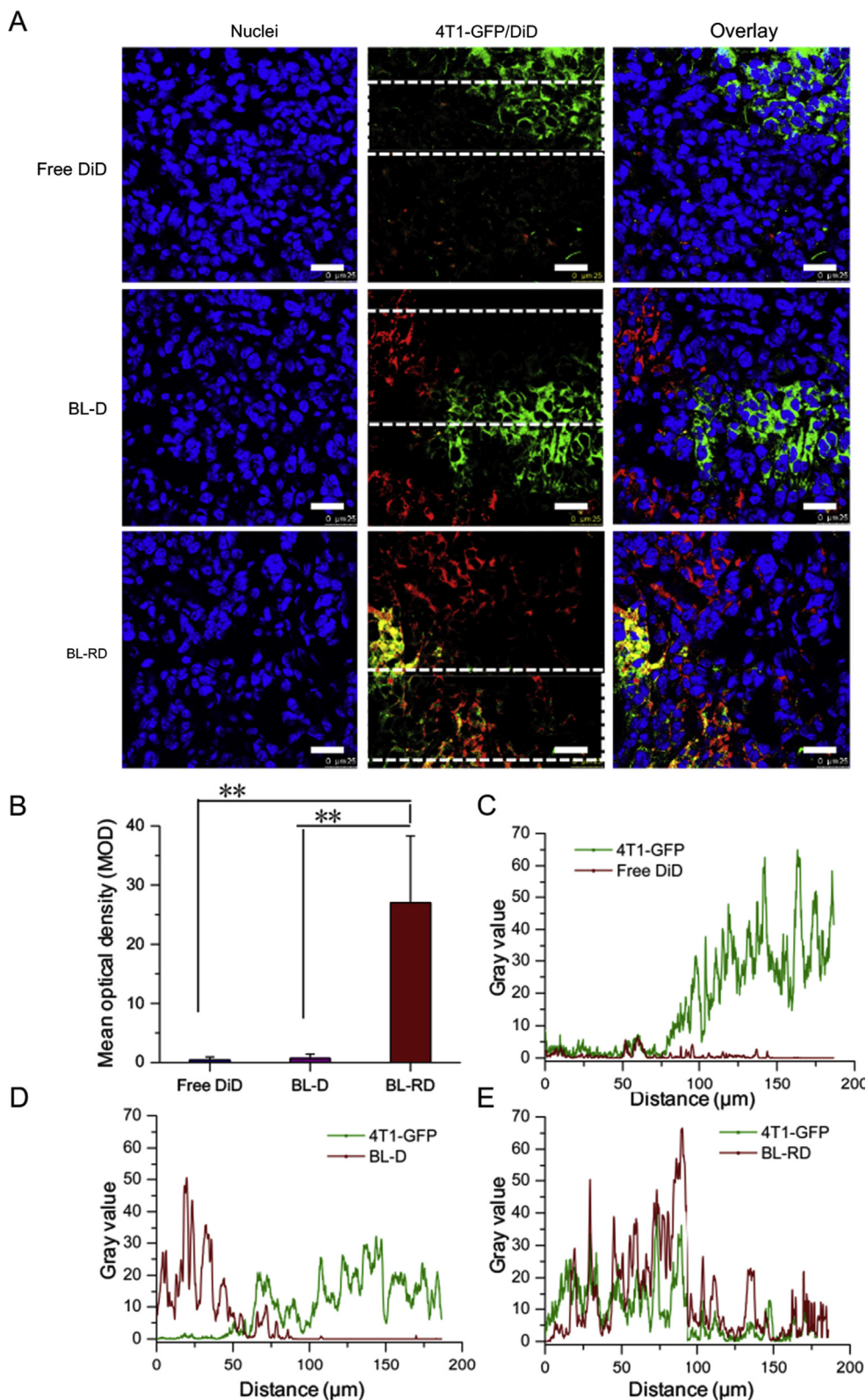
Figure 8 The *in vivo* accessing of BL-D and BL-RD to cancer cells in tumor sites. (A) The accessing of BL-D and BL-RD to cancer cells could be considered as the combination of green signals and red signals in the captured images under CLSM, scale bar=25 μm. (B) The mean fluorescence density of the red signals in 4T1-GFP cells regions. Data are mean±SD (*n*=3). $^{**}P<0.01$. (C) The image analysis of red and green signals in regions between two white lines in free DiD group. (D) The image analysis of red and green signals in regions between two white lines in BL-D group. (E) The image analysis of red and green signals in regions between two white lines in BL-RD group. The analysis was performed by image J software.
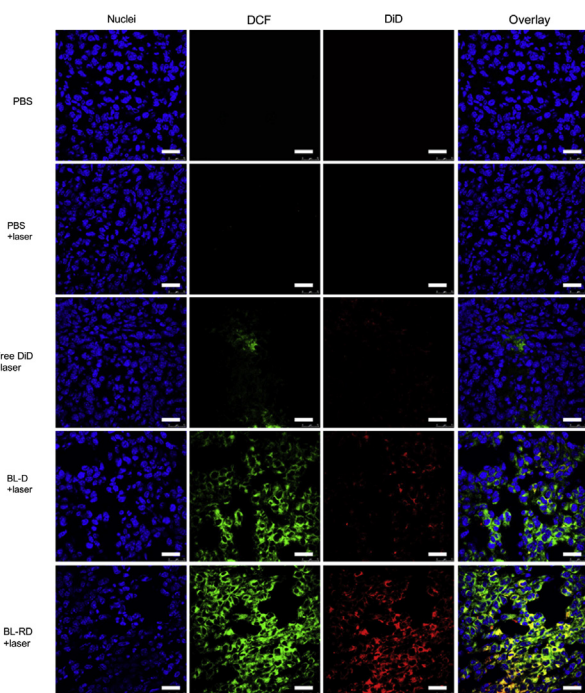
Figure 9 The production of ROS in tumor from free DiD, BL-D- and BL-RD-treated mice upon their exposure to 655 nm laser at 2.0 W/cm² for 2 min, scale bar = 25 μm. DCFH-DA was used as probe to monitor the production of ROS in tumor model.

were stained with specific antibodies to mark these cells, respectively, and detect their spatial targeting to various cells in the tumor (Fig. 7, Supporting Information Figs. S16 and S17). In the captured images, TAM was denoted as F4/80 positive cells (green signals), EC was expressed as CD31 positive cells (white signals), and CAF was referred as cells with α-SMA positive and CD31 negative expression (α-SMA⁺/CD31⁻, green signals excluding the white signals). The internalization of BL-RD, and BL-D by these stromal cells could be defined as the combination of red signals with the fluorescence signals of these stromal cells. As shown in Fig. 7, the red signals could be largely colocalized with the specific signals of TAM, CAF, and EC in BL-D group, suggesting their extensive uptake by these stromal cells in the tumor. However, in BL-RD-treated group, only part of the red signals was combined with these stromal cells and plenty of the red signals from BL-RD did not coincide with the signals of these stromal cells (Fig. 7). These results revealed the potential uptake of BL-RD by other cell fractions besides these stromal cells in tumor tissues.

Then, the accessing of BL-RD to cancer cells were determined in a tumor model induced by 4T1-GFP cancer cells. The accessing of BL-RD to cancer cells could be directly expressed as their localization in 4T1-GFP cells in the tumor. By contrast, the sections were stained with DAPI for the observations. In Fig. 8, the red signals from BL-D were mainly located distant away from the green fluorescence of 4T1-GFP cancer cells and negligibly observed in the clustered 4T1-GFP cell regions in the tumor. However, the red signals from BL-RD could feasibly reach the tumor regions with green fluorescence signals and largely distributed in these green fluorescence-marked cells. By contrast, the red signals of Lipo-RD were mildly detected in the 4T1-GFP cell regions and the fluorescence intensity was much lower than that of BL-RD (Supporting Information Fig. S18). These

observations confirmed the limited accessing of Lipo-D and BL-D to cancer cells and efficient cancer cells accessibility of BL-RD, thereby proving the superiority of BL-RD on enhancing its accessibility to cancer cell fractions in solid tumor. The image analysis results showed that the mean fluorescence intensity of BL-RD in the 4T1 cancer cell regions of tumor mass was 37.5-fold high than that of BL-D and 4.5-fold stronger than that of liposomal formulation of Lipo-RD. The enhanced cancer cell accessibility of BL-RD over BL-D could be mainly ascribed to the decoration of CRGDfK peptide in BL-RD, which effectively facilitate the flexible diffusion of BL-RD in tumor mass and provide an opportunity to recognize the cancer cells. The higher cancer cells accessibility of BL-RD over the Lipo-RD would be owing to the considerable enhancement of tumor accumulation. We have evidenced the preferential uptake of BL-RD in 4T1 cancer cell *via* specific interactions with the SR-BI and $\alpha_{v}\beta_{3/5}$ integrins in cancer cells (Figs. S7 and S9). In a short conclusion, the small particles, biomimetic properties and the surface decoration of CRGDfK peptide in BL-RD constituted of the major contributors for their efficient accessibility to the cancer cells in tumor tissues.

3.5. In vivo photodynamic activity of BL-RD and the combinational antitumor therapy

In view of the flexible permeation of BL-RD in tumor mass and their effective accessibility to cancer cells, the photodynamic activities of BL-RD in tumor were measured in comparison with BL-D in 4T1-induced tumor model. At 12 h postinjection of free DiD, BL-D and BL-RD, the ROS detection reagent of DCFH-DA was injected to tumor tissues at 2 mg/kg and the tumor sites were exposed to 655 nm laser at 2.0 W/cm² for 2 min. Twenty minutes later, mice were autopsied and the tumor tissues were carefully collected, frozen and sectioned for visualization under CLSM. By contrast, the tumor sections were stained with DAPI as control. The production of ROS was denoted as green signals in the captured images, which was largely detected with strong intensity in BL-D- and BL-RD-treated groups upon laser irradiation (Fig. 9), but rarely observed in these groups without laser irradiation (Supporting Information Fig. S19). Moreover, the green fluorescence signals of ROS have coincided with the red signals of BL-D or BL-RD, suggesting the high photodynamic activities of BL-D and BL-RD upon laser irradiation. In addition, the production of ROS was barely detected in PBS, PBS+laser, free DiD+laser groups (Fig. 9). Our finding firstly evidenced the *in vivo* photodynamic activity of DiD after its incorporation into the biomimetic lipoproteins of BL-D and BL-RD. The efficient production of ROS in BL-D- and BL-RD-treated groups could be attributed to their high accumulations in the tumor sites and deep tumor-penetrating capacity, which potentiated their applications in antitumor therapy.

Then, the therapeutic effect of BL-RD-mediated combinational therapy on tumor growth was evaluated in 4T1-induced tumor model (Fig. 10). When tumor volume reached approximately 150 mm³, mice were respectively injected with free DiD, BL-D, RM, and BL-RD at 5 mg/kg of DiD and 2 mg/kg of RM. In DiD, BL-D- and BL-RD-treated groups, the tumor sites were exposed to 655 nm laser at a power density of 2 W/cm² for 2 min at 12 h after injection. These mice were treated for a total of 3 times (Fig. 10A). The tumor growth and the body weights were supervised during these treatments (Fig. 10B and C, and Supporting Information Fig. S20). In the tumor growth profiles, the

tumor sizes were barely changed with time in BL-RD+laser group but gradually increased in other groups, suggesting the notable inhibition on tumor growth by the BL-RD-mediated chemo-photodynamic therapy. When comparing to the tumor volume in PBS control group, the tumor sizes were reduced by 28.9% in free RM groups and further decreased to about 57.6% in BL-RD group without laser irradiation. Similarly, in laser irradiated groups, the tumor volume was slightly reduced by 17.5% in free DiD+laser group and depressed around 55.8% in BL-D+laser group. These results effectively verified the enhanced therapeutic effects of the

active agents of RM or photosensitizer DiD after their entrapment into the biomimetic lipoproteins system. Particularly in the BL-RD+laser group, the tumor size was notably reduced by 84.7%, which was significantly higher than that of BL-RD and BL-D+laser group, validating the effectiveness of the BL-RD-mediated combinational chemo-photodynamic therapy. Meanwhile, the tumor growth index (TGI) that was denoted as the tumor volume at end time points compared to that at the initial time points were used to evaluate the inhibitory effects on tumor growth. The TGI was only 1.3 in the combinational BL-RD+laser
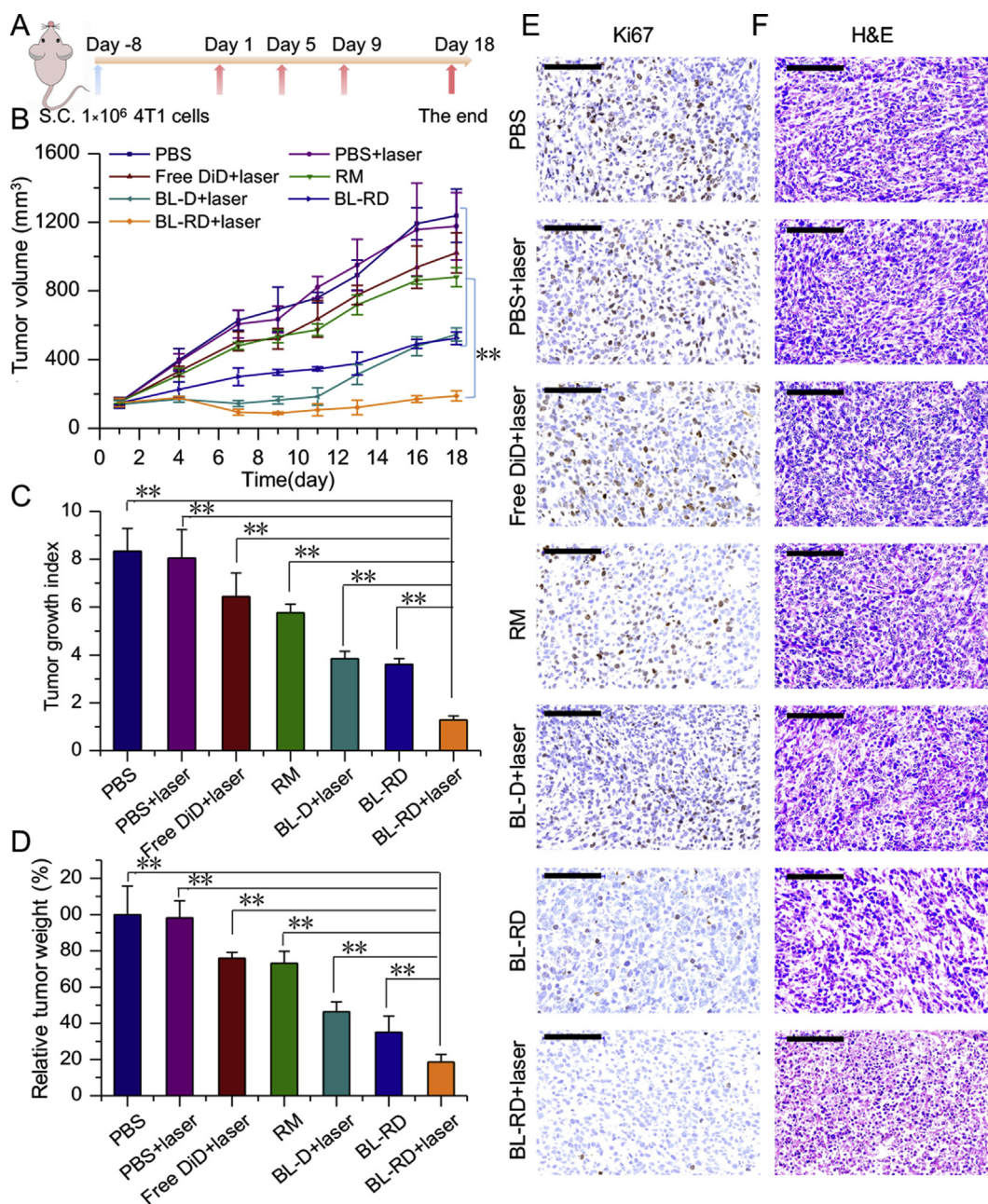
Figure 10 The *in vivo* therapeutic effects of BL-RD on tumor growth in 4T1-indcued breast cancer model. (A) The regimens of treatments. (B) The tumor growth profiles from each treatment. Data are mean±SD ($n=5$). **$P<0.01$. (C) The tumor growth index from each group at day 18 after first treatment, which was defined as the ratio of the tumor size at day 18 compared to that at the initial time point. Data are mean±SD ($n=5$). **$P<0.01$. (D) The relative tumor weight from each treatment. Data are mean±SD ($n=5$). **$P<0.01$. (E) The Ki67 expression in tumor from each group, scale bar＝100 μm. (F) The histological examination of tumor tissues from each group by H&E staining method, scale bar＝100 μm.

group, suggesting the remarkable inhibitory effects of BL-RD-mediated chemo-photodynamic therapy on tumor growth (Fig. 10C). Moreover, the drastic depression of BL-RD+laser on tumor growth was confirmed by measuring the tumor weights from each group (Fig. 10D and Supporting Information Fig. S21).

The proliferation of cancer cells in tumor tissues from each group was measured by Ki67 detections, which showed the remarkable reduction of cell proliferation by the BL-RD-mediated chemo-photodynamic therapy (Fig. 10E). Meanwhile, the histological examinations of the tumor tissues were performed by hematoxylin-eosin (HE) staining method, which showed the extensive incidence of cell membrane damage and cell nuclei pyknosis in BL-RD+laser-treated group (Fig. 10F). These results confirmed the effectiveness of BL-RD-mediated combinational therapy. As a result, the BL-RD-mediated chemo-photodynamic therapy could result in an exceeding inhibition on tumor growth, which was more effective than the BL-RD group without laser irradiation and the BL-D+laser treatments. The biomimetic lipoprotein system can be easily modified with different ingredients and surface modification, and load diverse imaging and therapeutic agents for combinational clinical applications[20−22]. The involvement of RM in BL-RD endowed them the superiority of flexible permeation across the tumor mass and efficient accessibility to cancer cells in tumor tissues. Meanwhile, the loading of DiD in the BL-RD system would improve its stability in the physiological fluids and potentiate their application in tumor imaging and photodynamic therapy. The combination of RM and DiD in the BL-RD system make it an encouraging nanoplatform with efficient cancer cells-accessing capability for combinational chemo-photodynamic therapy, thereby holding great premise for further clinical translational applications.

4. Conclusions

In summary, we rationally designed a cyclic CRGDfK peptide modified biomimetic lipoproteins system of BL-RD with deep tumor penetration and *in vivo* cancers-cell-accessing capacity for tumor therapy. The BL-RD system could load chemotherapeutic agents of RM and photosensitizer DiD for combinational chemo-photodynamic therapy of breast cancer. In a 4T1-induced tumor model, BL-RD displayed specific tumor accumulation, flexible permeation, and diffusion in tumor mass and effective accessibility to cancer cells in the tumor, thereby producing notable inhibition on tumor growth. Therefore, the rationally designed BL-RD provides a promising nanoplatform with efficient tumor-penetrating and cancer-cells-accessing capability for effective antitumor therapy.

Author contributions

Tao Tan and Yuqi Wang carried out the experiments and performed data analysis. Jing Wang and Zhiwan Wang developed the in vitro and in vivo experimental models. Hong Wang, Haiqiang Cao and Jie Li assited the in vivo therapeutic evalations. Tao Tan and Zhiwen Zhang designed the experiments, interpreted the data, and wrote the manuscript. Siling Wang and Yaping Li supervised the project and interpreted the data. All of the authors have read and approved the final manuscript.

Conflicts of interest

The authors have no conflicts of interest to declare.

Appendix A. Supporting information

Supporting data to this article can be found online at https://doi.org/10.1016/j.apsb.2019.05.006.

References

1. Shi J, Kantoff PW, Wooster R, Farokhzad OC. Cancer nanomedicine: progress, challenges and opportunities. *Nat Rev Canc* 2017;**17**:20−37.
2. Zhang Z, Wang H, Tan T, Li J, Wang Z, Li Y. Rational design of nanoparticles with deep tumor penetration for effective treatment of tumor metastasis. *Adv Funct Mater* 2018;**28**:1801840.
3. Min Y, Caster JM, Eblan MJ, Wang AZ. Clinical translation of nanomedicine. *Chem Rev* 2015;**115**:11147−90.
4. Gradishar WJ, Tjulandin S, Davidson N, Shaw H, Desai N, Bhar P, et al. Phase III trial of nanoparticle albumin-bound paclitaxel compared with polyethylated castor oil-based paclitaxel in women with breast cancer. *J Clin Oncol* 2005;**23**:7794−803.
5. Wilhelm S, Tavares AJ, Dai Q, Ohta S, Audet J, Dvorak HF, et al. Analysis of nanoparticle delivery to tumours. *Nat Rev Mater* 2016;**1**:16014.
6. Blanco E, Shen H, Ferrari M. Principles of nanoparticle design for overcoming biological barriers to drug delivery. *Nat Biotechnol* 2015;**33**:941−51.
7. Torok S, Rezeli M, Kelemen O, Vegvari A, Watanabe K, Sugihara Y, et al. Limited tumor tissue drug penetration contributes to primary resistance against angiogenesis inhibitors. *Theranostics* 2017;**7**:400−12.
8. Baslan T, Hicks J. Unravelling biology and shifting paradigms in cancer with single-cell sequencing. *Nat Rev Canc* 2017;**17**:557−69.
9. Yu M, Tannock IF. Targeting tumor architecture to favor drug penetration: a new weapon to combat chemoresistance in pancreatic cancer? *Cancer Cell* 2012;**21**:327−9.
10. Balkwill FR, Capasso M, Hagemann T. The tumor microenvironment at a glance. *J Cell Sci* 2012;**125**:5591−6.
11. Chauhan VP, Jain RK. Strategies for advancing cancer nanomedicine. *Nat Mater* 2013;**12**:958−62.
12. Miller MA, Gadde S, Pfirschke C, Engblom C, Sprachman MM, Kohler RH, et al. Predicting therapeutic nanomedicine efficacy using a companion magnetic resonance imaging nanoparticle. *Sci Transl Med* 2015;**7**:314ra183.
13. Wang L, Hu Y, Hao Y, Li L, Zheng C, Zhao H, et al. Tumor-targeting core-shell structured nanoparticles for drug procedural controlled release and cancer sonodynamic combined therapy. *J Control Release* 2018;**286**:74−84.
14. Xu L, Tong G, Song Q, Zhu C, Zhang H, Shi J, et al. Enhanced intracellular Ca^{2+} nanogenerator for tumor-specific synergistic therapy *via* disruption of mitochondrial Ca^{2+} homeostasis and photothermal therapy. *ACS Nano* 2018;**12**:6806−18.
15. Nel A, Ruoslahti E, Meng H. New insights into "permeability" as in the enhanced permeability and retention effect of cancer nanotherapeutics. *ACS Nano* 2017;**11**:9567−9.
16. Liu R, Hu C, Yang Y, Zhang J, Gao H. Theranostic nanoparticles with tumor-specific enzyme-triggered size reduction and drug release to perform photothermal therapy for breast cancer treatment. *Acta Pharm Sin B* 2019;**9**:410−20.

17. Dai Q, Wilhelm S, Ding D, Syed AM, Sindhwani S, Zhang Y, et al. Quantifying the ligand-coated nanoparticle delivery to cancer cells in solid tumors. *ACS Nano* 2018;**12**:8423−35.

18. Miller MA, Zheng YR, Gadde S, Pfirschke C, Zope H, Engblom C, et al. Tumour-associated macrophages act as a slow-release reservoir of nano-therapeutic Pt(IV) pro-drug. *Nat Commun* 2015;**6**:8692.

19. Miao L, Newby JM, Lin CM, Zhang L, Xu F, Kim WY, et al. The binding site barrier elicited by tumor-associated fibroblasts interferes disposition of nanoparticles in stroma-vessel type tumors. *ACS Nano* 2016;**10**:9243−58.

20. Ng KK, Lovell JF, Zheng G. Lipoprotein-inspired nanoparticles for cancer theranostics. *Acc Chem Res* 2011;**44**:1105−13.

21. Kuai R, Li D, Chen YE, Moon JJ, Schwendeman A. High-density lipoproteins: nature's multifunctional nanoparticles. *ACS Nano* 2016;**10**:3015−41.

22. Mulder WJ, van Leent MM, Lameijer M, Fisher EA, Fayad ZA, Pérez-Medina C. High-density lipoprotein nanobiologics for precision medicine. *Acc Chem Res* 2018;**51**:127−37.

23. Kuai R, Ochyl LJ, Bahjat KS, Schwendeman A, Moon JJ. Designer vaccine nanodiscs for personalized cancer immunotherapy. *Nat Mater* 2017;**16**:489−96.

24. Ma X, Song Q, Gao X. Reconstituted high-density lipoproteins: novel biomimetic nanocarriers for drug delivery. *Acta Pharm Sin B* 2018;**8**:51−63.

25. He X, Bao X, Cao H, Zhang Z, Yin Q, Gu W, et al. Tumor-penetrating nanotherapeutics loading a near-infrared probe inhibit growth and metastasis of breast cancer. *Adv Funct Mater* 2015;**25**:2831−9.

26. Cabral H, Matsumoto Y, Mizuno K, Chen Q, Murakami M, Kimura M, et al. Accumulation of sub-100 nm polymeric micelles in poorly permeable tumours depends on size. *Nat Nanotechnol* 2011;**6**:815−23.

27. Hu H, Wang J, Wang H, Tan T, Li J, Wang Z, et al. Cell-penetrating peptide-based nanovehicles potentiate lymph metastasis targeting and deep penetration for anti-metastasis therapy. *Theranostics* 2018;**8**:3597−610.

28. Ruan S, Qian J, Shen S, Chen J, Cun X, Zhu J, et al. Non-invasive imaging of breast cancer using RGDyK functionalized fluorescent carbonaceous nanospheres. *RSC Adv* 2015;**5**:25428−36.

29. Hu G, Zhang H, Zhang L, Ruan S, He Q, Gao H. Integrin-mediated active tumor targeting and tumor microenvironment response dendrimer-gelatin nanoparticles for drug delivery and tumor treatment. *Int J Pharm* 2015;**496**:1057−68.

30. Zeng L, Zou L, Yu H, He X, Cao H, Zhang Z, et al. Treatment of malignant brain tumor by tumor-triggered programmed wormlike micelles with precise targeting and deep penetration. *Adv Funct Mater* 2016;**26**:4201−12.

31. Cui L, Lin Q, Jin CS, Jiang W, Huang H, Ding L, et al. A PEGylation-free biomimetic porphyrin nanoplatform for personalized cancer theranostics. *ACS Nano* 2015;**9**:4484−95.

32. Kadiyala P, Li D, Nuñez FM, Altshuler D, Doherty R, Kuai R, et al. High-density lipoprotein-mimicking nanodiscs for chemo-immunotherapy against glioblastoma multiforme. *ACS Nano* 2019;**13**:1365−84.

33. Kuai R, Yuan W, Son S, Nam J, Xu Y, Fan Y, et al. Elimination of established tumors with nanodisc-based combination chemo-immunotherapy. *Sci Adv* 2018;**4**:eaao1736.

34. Cao H, Dan Z, He X, Zhang Z, Yu H, Yin Q, et al. Liposomes coated with isolated macrophage membrane can target lung metastasis of breast cancer. *ACS Nano* 2016;**10**:7738−48.

35. Parvani JG, Galliher-Beckley AJ, Schiemann BJ, Schiemann WP. Targeted inactivation of $\beta 1$ integrin induces $\beta 3$ integrin switching, which drives breast cancer metastasis by TGF-β. *Mol Biol Cell* 2013;**24**:3449−59.

36. Doolittle E, Peiris PM, Doron G, Goldberg A, Tucci S, Rao S, et al. Spatiotemporal targeting of a dual-ligand nanoparticle to cancer metastasis. *ACS Nano* 2015;**9**:8012−21.

37. Hu C, Yang X, Liu R, Ruan S, Zhou Y, Xiao W, et al. Coadministration of iRGD with multistage responsive nanoparticles enhanced tumor targeting and penetration abilities for breast cancer therapy. *ACS Appl Mater Interfaces* 2018;**10**:22571−9.

38. Yan F, Xu X, Chen Y, Deng Z, Liu H, Xu J, et al. A lipopeptide-based $\alpha_v \beta_3$ integrin-targeted ultrasound contrast agent for molecular imaging of tumor angiogenesis. *Ultrasound Med Biol* 2015;**41**:2765−73.

39. Majkowski M, Póda P, Kulbacka J, Saczko J, Sikorski AF. Alternation of fluorescent spectra of membrane markers DiI C18(3) and DiI C18(5) evoked by laser illumination. *J Histochem Cytochem* 2012;**60**:789−91.

40. He B, Hu HY, Tan T, Wang H, Sun KX, Li YP, et al. IR-780-loaded polymeric micelles enhance the efficacy of photothermal therapy in treating breast cancer lymphatic metastasis in mice. *Acta Pharmacol Sin* 2018;**39**:132−9.

41. Schweitzer C, Schmidt R. Physical mechanisms of generation and deactivation of singlet oxygen. *Chem Rev* 2003;**103**:1685−757.

42. Hong EJ, Choi DG, Shim MS. Targeted and effective photodynamic therapy for cancer using functionalized nanomaterials. *Acta Pharm Sin B* 2016;**6**:297−307.

43. Duan X, Li Y. Physicochemical characteristics of nanoparticles affect circulation, biodistribution, cellular internalization, and trafficking. *Small* 2013;**9**:1521−32.

44. Wang J, Mao W, Lock LL, Tang J, Sui M, Sun W, et al. The role of micelle size in tumor accumulation, penetration, and treatment. *ACS Nano* 2015;**9**:7195−206.

45. Mallidi S, Anbil S, Bulin AL, Obaid G, Ichikawa M, Hasan T. Beyond the barriers of light penetration: strategies, perspectives and possibilities for photodynamic therapy. *Theranostics* 2016;**6**:2458−87.

46. Wu H, Yu M, Miao Y, He S, Dai Z, Song W, et al. Cholesterol-tuned liposomal membrane rigidity directs tumor penetration and anti-tumor effect. *Acta Pharm Sin B* 2019;**9**:858−70.

47. Wang R, Shen Q, Li X, Xie C, Lu W, Wang S, et al. Efficacy of inverso isomer of CendR peptide on tumor tissue penetration. *Acta Pharm Sin B* 2018;**8**:825−32.

48. Tan T, Wang H, Cao H, Zeng L, Wang Y, Wang Z, et al. Deep tumor-penetrated nanocages improve accessibility to cancer stem cells for photothermal-chemotherapy of breast cancer metastasis. *Adv Sci* 2018;**5**:1801012.

49. Insua-Rodríguez J, Oskarsson T. The extracellular matrix in breast cancer. *Adv Drug Deliv Rev* 2016;**97**:41−55.

50. Kalluri R. The biology and function of fibroblasts in cancer. *Nat Rev Canc* 2016;**16**:582−98.

51. Dewhirst MW, Secomb TW. Transport of drugs from blood vessels to tumour tissue. *Nat Rev Canc* 2017;**17**:738−50.

52. Cao H, Wang H, He X, Tan T, Hu H, Wang Z, et al. Bioengineered macrophages can responsively transform into nanovesicles to target lung metastasis. *Nano Lett* 2018;**18**:4762−70.

53. He X, Cao H, Wang H, Tan T, Yu H, Zhang P, et al. Inflammatory monocytes loading protease-sensitive nanoparticles enable lung metastasis targeting and intelligent drug release for anti-metastasis therapy. *Nano Lett* 2017;**17**:5546−54.